

Alumina-grafted SBA-15 as a high performance support for Pd-catalysed cinnamyl alcohol selective oxidation

Christopher M.A. Parlett, Lee J. Durndell, Andreia Machado, Giannantonio Cibin, Duncan W. Bruce, Nicole S. Hondow, Karen Wilson, Adam F. Lee* (a.f.lee@aston.ac.uk)

1. Introduction

Cinnamaldehyde is an allylic aldehyde widely employed as a chemical intermediate in organic synthesis and as a desirable product in its own right for application as an insecticide and food and perfume additive [1]. Related aromatic and aliphatic allylic aldehydes are also commercially important fine chemical and agrochemical products [2], [3] and [4], hence their green synthesis through low-energy and atom-economical routes has been the focus of extensive academic and commercial research. The direct aerobic selective oxidation (selox) of allylic alcohols is a potential route to such unsaturated aldehydes that avoids recourse to stoichiometric oxidants and can be undertaken in either the liquid or vapour phase under mild conditions [5] and [6]. Such chemistry is believed to proceed via oxidative dehydrogenation of the alcohol to the corresponding allylic aldehyde which may undergo subsequent oxidation to the acid. Aldehyde selectivity is also influenced by competitive hydrogenation of the Cdouble bond; length as m-dashC bond or Csingle bondO cleavage in the parent alcohol, and decarbonylation of the desired aldehyde product.

A number of heterogeneous catalysts capable of facilitating alcohol selox using air or dioxygen as the oxidant have been developed, with nanoparticulate palladium and/or gold the active components of choice [7], [8], [9], [10] and [11]. In recent years, an array of ex situ and in situ analytical techniques and parallel kinetic profiling has identified electron-deficient Pd²⁺, present as PdO at the surface of nanoparticles, as the active species participating in palladium-catalysed allylic alcohol selox. Pd²⁺ species are proposed to play a critical role in aerobic alcohol oxidations over AuPd core-shell nanoparticles [12] and intercalated Pd/NiZn layered double hydroxides [13], while Pd²⁺ complexes are ubiquitous in homogeneously catalysed selox chemistry [14] and [15]. Time-resolved, liquid and vapour phase XAS measurements [16], [17], [18] and [19] on carbon and oxide supported nanoparticles respectively, and complementary in situ XPS measurements over O/Pd(1 1 1) single crystals [20] and [21] have highlighted PdO reduction to metallic palladium as a potential deactivation pathway, and hence the importance of generating highly dispersed nanoparticles which favour an oxide phase [20], [22], [23] and [24]. Temperature-programmed desorption and XPS of crotyl alcohol (but-2-en-1-ol) and crotonaldehyde (but-2-en-1-al) over Pd(1 1 1) and palladium-rich Au/Pd surface alloys suggest deactivation arises from crotonaldehyde decarbonylation and subsequent site-blocking by strongly adsorbed propylidyne and CO [20] and [21]. Computational modelling predicts Pd(1 1 1) can also drive propanoic acid decarbonylation [25]. Vapour phase studies of crotyl alcohol oxidation show that such in situ palladium reduction is reversible under oxidising environments [17] and [19], enabling selox to be maintained, however the ability of dissolved oxygen to preserve palladium as PdO during liquid phase selox is unknown.

Improved palladium selox catalysts require enhanced surface PdO concentration. A number of approaches have been explored to disperse palladium nanoparticles throughout nanoporous supports, e.g. Pd coordination to pyridyls [26] or amines [27] and [28] covalently tethered to silicas. However, the grafting densities achievable via such organic surface functionalisation are low (typically 0.1 ligands nm⁻²), and palladium is only weakly bound and prone to leaching in situ. Direct impregnation of inorganic oxides with palladium precursors (and subsequent thermochemical processing) or pre-formed colloidal nanoparticles remain the simplest, scalable routes to achieving high Pd dispersion, although the presence of surfactant/polymer stabilisers can hinder good adhesion of pre-prepared colloids and/or modify their catalytic reactivity [29]. Tailoring the support architecture offers an alternative means to influencing palladium dispersion. Ordered mesoporous silicas, prepared via surfactant templating routes [30] and [31], possess high surface areas and interconnected mesopores that permit the synthesis of highly oxidised

1–2 nm Pd particles [22] and [23]. We recently discovered that mesoporous alumina is superior to silica for stabilising sub-nanometre palladium clusters and even atomically dispersed Pd²⁺ centres [24] and [32], presumably reflecting a stronger metal-support interaction (a function of the acid/base character of metal oxides [33], [34] and [35]). Unfortunately, pure alumina supports are plagued by low hydrothermal stability, and typically significantly lower surface areas and mesopore ordering than their silica counterparts. The growth of conformal alumina coatings over a mesostructured silica framework opens the way to new catalyst supports combining the structural stability (and diverse topologies) accessible through silica materials chemistry, with the surface chemistry of alumina. Alumina coated MCM-41 [36] and SBA-15 [37] have been reported via hydrolysis of alkoxyaluminium species. Such dual-oxide supports have shown enhanced immobilisation of heteropoly acids [38] and attendant activity in o-xylene alkylation [39], and strong metal support interactions in bimetallic PtSn catalysts promoting propane dehydrogenation [40]. Alumina grafting also affords a direct means to introduce surface acidity into silica [41] and thus control activity and selectivity in cobalt-catalysed Fischer–Tropsch synthesis [42].

Here we report the first use of alumina-functionalised, mesoporous silica as a support for catalytic oxidation. Palladium-impregnated Al-SBA-15 exhibits significantly higher nanoparticle dispersions and surface PdO concentrations than either pure mesoporous alumina or SBA-15 supports, and correspondingly higher activities in the liquid phase aerobic selox of cinnamyl alcohol to cinnamaldehyde. Complementary operando XAS measurements reveal a strong correlation between activity and in situ palladium oxidation state, with dissolved oxygen maintaining an active PdO species and thereby retarding on-stream catalyst deactivation.

2. Experimental

2.1. Catalyst synthesis

The parent SBA-15 silica framework was synthesised following the method of Zhao et al. [30]. Pluronic P123 (10 g) was dissolved in water (75.5 cm³) and HCl (2 M, 291.5 cm³) and stirred at 35 °C. Tetramethoxysilane (15.5 cm³) was then added, and the mixture left for 20 h under agitation. The resulting gel was aged for 24 h at 100 °C without agitation. The remaining solid was filtered, washed with water (1000 cm³) and dried at room temperature before calcining at 500 °C for 6 h under flowing air (ramp rate 1 °C min⁻¹). The protocol of Landau and co-workers was used to deposit a uniform alumina coating onto SBA-15 (Al-SBA-15(n) where n corresponds to the number of grafting cycles) [36]. Aluminium-tri-sec-butoxide (14.5 g) was dissolved in anhydrous toluene (100 cm³) at 85 °C with stirring. Triethylamine (2.1 cm³) was added to the solution followed by dried SBA-15 (1 g). After 6 h stirring at 85 °C the solution was filtered under vacuum (~0.1 bar) to recover the solid, which was washed three times with toluene (or 3 × 35 cm³ total). The alumina precursor was hydrolysed in ethanol (318 cm³) containing water (1.6 cm³) for 24 h at 25 °C. The solid product was recovered by filtration under vacuum (~0.1 bar), washed with ethanol (300 cm³), and dried under vacuum (0.25 bar) at 50 °C on a rotary evaporator. The solid was further dried at 120 °C in air, before a three-step calcination sequence. The powdered material was initially heated to 250 °C for 1 h, then 400 °C for 1 h and finally 500 °C for 4 h (common ramp rate 1 °C min⁻¹). Consecutive alumina grafting cycles were carried out using an identical protocol each time, with adjustments to the quantities to maintain the initial Al:Si ratios.

A nominal 1 wt.% Pd/Al-SBA-15(4) catalyst was prepared using tetraamine palladium(II) nitrate solution (10 wt.% Pd salt) by incipient wetness impregnation. A slurry of the palladium precursor and Al-SBA-15(4) support was stirred for 18 h at room temperature before heating to 50 °C. After ~5 h, agitation was ceased and the solids aged at 50 °C for a further 24 h to yield a dry powder. Dried samples were calcined at 500 °C (ramp rate 1 °C min⁻¹) in static air for 2 h, then reduced under flowing H₂ (10 cm³ min⁻¹) at 400 °C (ramp rate 10 °C min⁻¹) for 2 h. The resulting materials were stored in air, and not re-activated prior to use. Full synthesis, characterisation and reactivity of Pd/SBA-15 and Pd/meso-Al₂O₃ controls are described in references [22], [23] and [24].

2.2. Catalyst characterisation

Accurate Pd loadings were determined by MEDAC Analytical and Chemical Consultancy Service Ltd. Samples were digested in HF prior to ICP analysis on a Varian Vista MPX inductively coupled plasma-optical emission spectrometer (ICP-OES).

Nitrogen porosimetry was undertaken on a Quantachrome Nova 2000e porosimeter, with analysis carried out using NovaWin v11 software. Samples were degassed at 120 °C for 2 h prior to recording N₂ adsorption/desorption isotherms. BET surface areas were calculated over the relative pressure range 0.02–0.2, with microporosity assessed by the t-plot method over the relative pressure range of 0.2–0.5; a linear relationship was observed for both. Pore diameters and volumes were calculated applying the BJH method to the desorption isotherm for relative pressures >0.35.

Powder X-ray diffraction (XRD) patterns were recorded on a Panalytical X'pertPro diffractometer fitted with an X'celerator detector using Cu K_α (1.54 Å) sources calibrated against a crystalline Si standard. Low-angle patterns were recorded for 2θ = 0.3–8° with a step size of 0.01°. Wide-angle patterns were recorded for 2θ = 25–75° with a step size of 0.02.

Pd dispersions were estimated by CO chemisorption on a Quantachrome ChemBET 3000 assuming a 1:2 CO:Pd stoichiometry. Samples were outgassed at 150 °C under flowing He (20 cm³ min⁻¹) for 1 h, then reduced at 100 °C under flowing hydrogen (20 cm³ min⁻¹) for 1 h before room temperature analysis. This reduction protocol is far milder than that employed during the catalyst synthesis, and hence does not induce particle sintering.

High-resolution (scanning) transmission electron microscopy (S)TEM images were recorded on a FEI Tecnai F20 FEG TEM operating at 200 kV equipped with a Gatan Orius SC600A CCD camera. Samples were prepared by dispersion in methanol and drop-casting onto a copper grid coated with a holey carbon support film (Agar Scientific Ltd). Images were analysed using ImageJ 1.41 software. High-angle annular dark-field (HAADF) imaging, which is particularly sensitive to heavy atoms [43], was used to image Pd-impregnated supports. Scanning electron microscopy (SEM) images were recorded on a Carl Zeiss Evo-40 SEM operating at 25 kV. Samples were supported on aluminium stubs each backed with carbon tape.

X-ray photoelectron spectra were acquired on a Kratos AXIS HSi spectrometer equipped with a charge neutraliser and monochromated Al K_α excitation source (1486.7 eV). Binding energy (BE) referencing was employed using the adventitious carbon peak at 284.6 eV. Survey scans were recorded for surface elemental analysis (pass energy 160 eV), with high resolution spectra recorded at 40 eV pass energy. Spectral fitting was performed using CasaXPS Version 2.3.5. A common Gaussian/Lorentzian (90:10) mix with asymmetry based on a Donaich-Sunjic mix of 0.005 was determined from fitting a PdO standard, and used for all Pd chemical environments, with a common full-width half maximum (FWHM) adopted for all components. Two Pd 3d_{5/2} species were observed at 335.4 and 336.8 eV, assigned as Pd metal and PdO respectively, both with spin-orbit doublet separations of 5.3 eV. It is important to recall that the inelastic mean free path of Pd 3d_{5/2} photoelectrons excited by Al K_α radiation is ~1.3 nm, i.e. comparable to the diameter of our nanoparticles, hence significant contributions may be expected from palladium metal residing within nanoparticle cores. Spectral fitting of Si, Al and O species was undertaken adopting a common Gaussian/Lorentzian (70:30) lineshape and FWHM. A maximum of two Si and two Al components were observed, assigned to the pure oxide and interfacial alumina-silicate species, at 103.4 and 102.3 eV for Si, and 73.8 and 74.7 eV for Al, with spin-orbit doublet separations of 0.61 eV (Si) and 0.41 eV (Al). O 1s XP spectra were fit to three components associated with the silica framework, alumina coating and alumina-silicate interface at 532.9, 530.9 and 531.8 eV respectively. All binding energies and doublet separations are consistent with those reported in the NIST surface database [44].

2.3. Cinnamyl alcohol selox

Catalyst screening was performed using a Radleys Starfish carousel batch reactor on a 10 cm³ scale at 90 °C under either static oxygen (1 bar), or with oxygen bubbled through the reaction solution (3 cm³ min⁻¹ at 1 bar) via 0.5 mm

i.d. PTFE tubing while magnetic stirring was maintained at 1000 rpm. 50 mg of catalyst was added to a reaction mixture of 8.4 mmol cinnamyl alcohol (1.123 g, Aldrich), 0.1 cm³ mesitylene (Aldrich) as an internal standard, and 10 cm³ HPLC grade toluene solvent. Control reactions in the absence of any solid phase, or presence of bare supports, were conducted in parallel, and all gave negligible conversions. Reactions were periodically sampled, with 0.25 cm³ aliquots withdrawn, filtered, and diluted with 1.75 cm³ toluene for triplicate analysis on a Varian 3900GC with CP-8400 autosampler (CP-Sil5 CB column, 15 m × 0.25 mm × 0.25 μm). Initial rates were calculated from the early linear region of the alcohol conversion profiles (typically 20–30 min reaction), with selectivity and mass balances calculated using calibrated response factors for reactants and products. Conversion and selectivity values are reported within ±3% error, with mass balances in all cases ≥95% during the first hour and ≥90% after 24 h.

2.4. Operando selox XAS measurements

Fluorescence Pd K-edge (24.35 KeV) X-ray absorption spectra were collected at Diamond Light Source on beamline B18 employing a Si [3 1 1] monochromator, Pt coated mirrors and a Vortex multichannel fluorescence detector. Operando XAS spectra were continuously acquired over a 4 h time period, spectra acquisition length of ~0.15 h, using a bespoke PTFE operando cell fitted with 25 μm Kapton windows. A reaction slurry of 250 mg catalyst, 84 mmol cinnamyl alcohol (11.23 g), 50 cm³ solvent and 0.5 cm³ mesitylene was continuously circulated through the cell via PTFE transfer tubing from a stirred glass reaction reservoir held at 90 °C under either static or flowing O₂ through the reaction solution (15 cm³ min⁻¹ at 1 bar) with magnetic stirrer at 1000 rpm. These reaction conditions represent a doubling of the alcohol:catalyst ratio with respect to the laboratory selox conditions above in order to observe the impact of oxygen upon deactivation processes over a reasonable timescale. Spectra were processed using the IFEFFIT version 1.2.11d open source software suite, employing Athena version 0.9.1 for normalisation, background subtraction and linear combination fitting of XANES, and Artemis version 0.9.1 for EXAFS fitting. Reference spectra of PdO and a Pd foil standard were also recorded.

3. Results and discussion

3.1. Material characterisation

Successful synthesis of the parent SBA-15 mesoporous silica support, which exists in a characteristic p6mm space group [30], and its retention following alumina grafting was first confirmed by low-angle XRD and nitrogen adsorption isotherms shown in Fig. 1. XRD patterns were essentially unchanged after the grafting procedure (Fig. 1A), with common reflections and peak intensities evidencing ordered mesostructures that were stable against pore expansion/contraction and collapse during the additional chemical and thermal processing associated with alumina coating. Porosimetry showed type IV isotherms with H1 hysteresis for SBA-15 and all Al-SBA-15 samples (Fig. 1B), highlighting the presence of mesopores. The corresponding surface areas decreased with alumina grafting cycle (Fig. 1C), due to initial micropore filling and subsequent loss of mesopore area coincident with shrinking mesopore diameter (WBJH). The latter is clear from the downshift in the unimodal BJH pore size distributions (Fig. 1D), with mesopores narrowing by 0.6 nm between the parent SBA-15 and Al-SBA-15(4). The constant unit cell parameter *a* (calculated from $a = 2d_{(100)}/\sqrt{3}$ for hexagonal close-packed mesopores, with the plane spacing *d* obtained from Bragg's Law) determined by XRD and narrowing mesopore diameters upon grafting, provide strong evidence for uniform alumina deposition within the mesopore matrix, apparent from the increase in wall thickness (*a* - *W*_{BJH}) with grafting cycle in Fig. 1E.

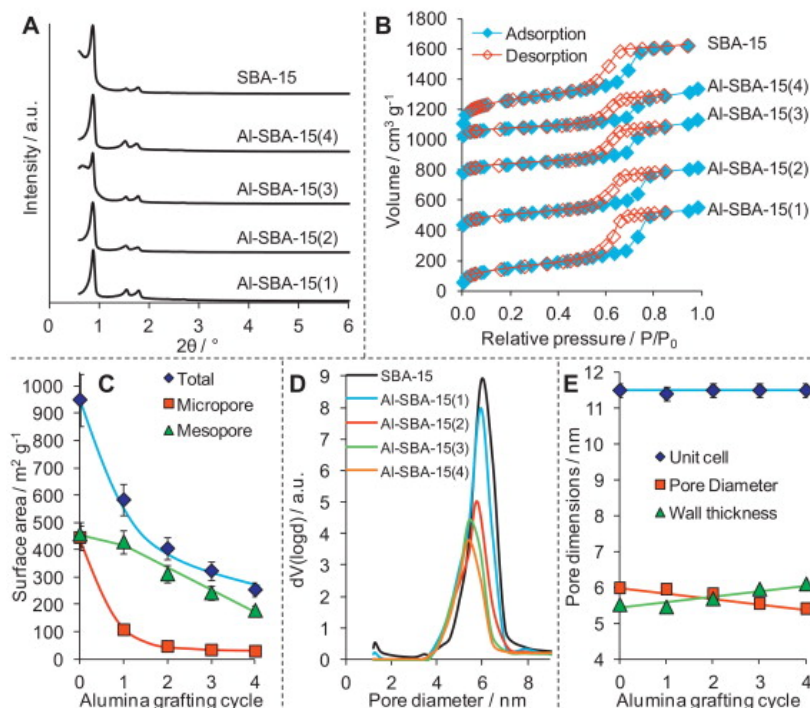


Fig. 1. - Structural properties of SBA-15 and Al-SBA-15 composites: (A) low angle XRD patterns; (B) N₂ adsorption isotherms; (C) surface areas (total from BET, micropore from t-plot, and mesopore from BET-micropore- external surface area); (D) BJH mesopore distribution; and (E) mesopore dimensions.

SEM images of the corresponding SBA-15 template and Al-SBA-15(4) material show a single, common straw-like crystallite morphology with matching dimensions (Fig. 2), precisely as anticipated if alumina had grafted into the parent SBA-15 framework, and not a second, discrete morphology that would indicate the formation of a separate, pure alumina phase.

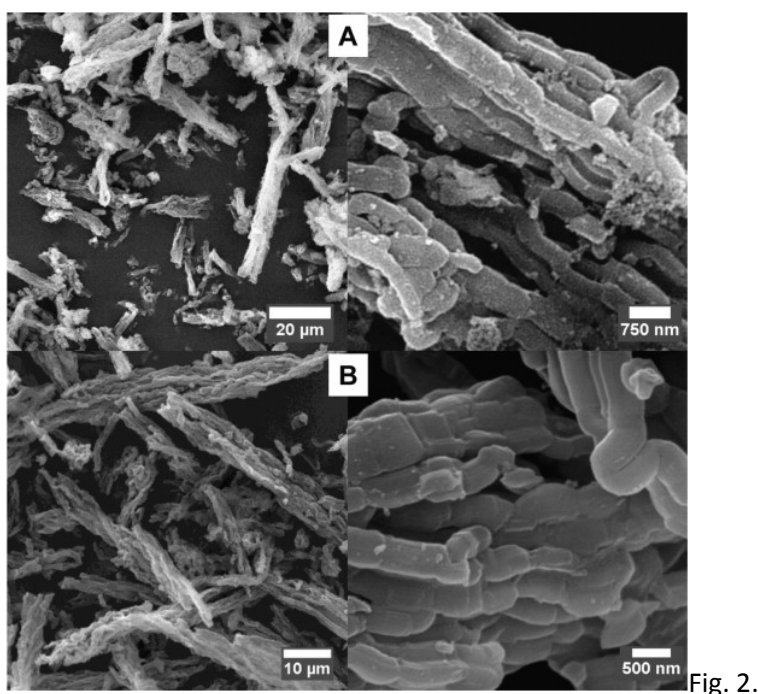


Fig. 2.

Fig. 2 Representative SEM images of (A) Al-SBA-15(4); and (B) the parent SBA-15.

The high surface sensitivity and chemical specificity of XPS renders it the ideal technique with which to follow the formation of alumina adlayers as a function of grafting number. As noted in the Experimental, the Al 2p, Si 2p and O 1s spectra for the Al-SBA-15 materials exhibit multiple chemical states associated with the underlying silica template,

alumina-silica interface, and alumina multilayers, as highlighted in Fig. 3. Aluminium and silicon atoms at the interface can be readily differentiated, since they exhibit unique BEs reflecting their different Pauling electronegativities and associated induced dipoles mediated via the bridging oxygen. Considering the Al 2p XP spectra (Fig. 3B), aluminium atoms within Al-SBA-15(1), i.e. deposited during the first grafting cycle, exhibit BE characteristic of Al³⁺ but occur at 74.7 eV, approximately 1.1 eV higher energy than observed for the pure mesoporous alumina (meso-Al₂O₃) reference. The absence of any bulk alumina features for Al-SBA-15(1) discounts the possibility that aluminium introduced during the grafting procedure is hydrolysed to an alumina phase spatially-isolated from the SBA-15 framework. The intensity of this interfacial alumina feature grows with each successive grafting cycle, and is accompanied by the emergence of bulk alumina features, consistent with the formation of alumina multilayers not in direct contact with the silica support. The converse behaviour is observed in the Si 2p XP spectra (Fig. 3A), wherein the pure parent SBA-15 component at 103.4 eV is progressively attenuated with each grafting cycle, concomitant with the growth of a new silicon environment at 102.3 eV attributed to electronically perturbed silicon atoms at the interface with the evolving alumina overlayer. The stoichiometry of the alumina coating was estimated from the ratio of the ‘bulk-like’ Al 2p_{3/2} state at 73.3 eV to the associated O 1s state at 530.9 eV, corrected for their relative instrumental response factors, and was between Al₂O_{2.9} and Al₂O_{3.2} demonstrating the successful deposition of a stoichiometric alumina adlayer. The thickness of the alumina overlayer can be estimated from the variation in the overall Si 2p XP intensity with excitation source energy. The inelastic mean free path for Si 2p_{3/2} photoelectrons excited by Mg K_α radiation is 2 nm versus 2.33 nm for excitation by Al K_α [45]. Applying these values to the Al-SBA-15(4) sample according to Eq. S1 (derived from [46]) yields an alumina thickness of 0.62 nm, which equates to ~2.7 alumina monolayers assuming a thickness of 0.23 nm [47], slightly greater than the pore shrinkage determined by porosimetry.

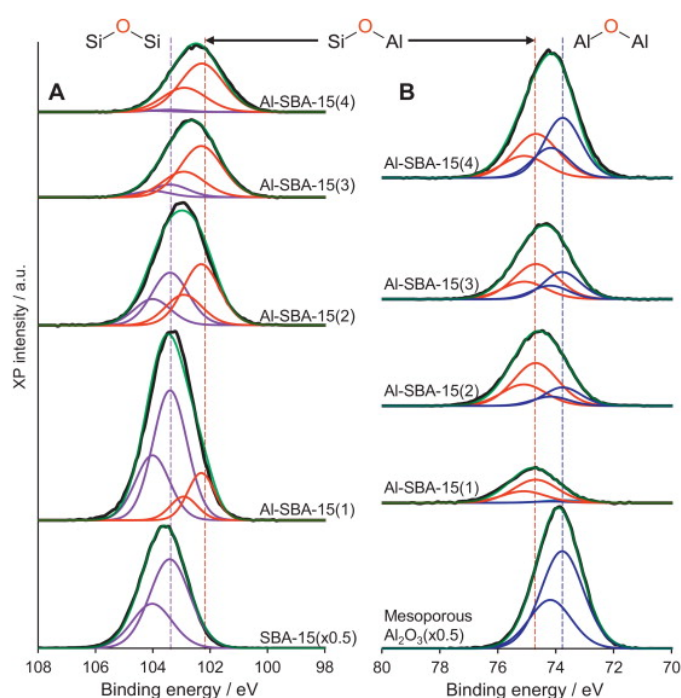


Fig. 3. Background-subtracted, fitted (A) Si 2p; and (B) Al 2p XP spectra of Al-SBA-15 as a function of alumina grafting cycles. Comparative spectra for SBA-15 and mesoporous alumina references are also shown.

Having established that the Al-SBA-15(4) material comprised a 2–3 monolayer, stoichiometric alumina coating permeating throughout the SBA-15 template, palladium nanoparticles were subsequently introduced via incipient wetness impregnation to achieve a loading of 0.77 wt.%. Low-angle XRD, porosimetry and XPS (Fig. S1) showed that the ordered mesostructure and alumina surface composition of the alumina-coated SBA-15 support were preserved in the resulting Pd/Al-SBA-15(4) sample. This contrasts with palladium incorporation by an identical protocol into a mesoporous alumina support, wherein alumina crystallisation and a consequent loss of mesopore ordering and pore dimensions was observed (Fig. S2), highlighting the greater stability of the Al-SBA-15 support.

Palladium nanoparticles and their size distribution and dispersion were evaluated by HAADF-STEM and CO chemisorption (Fig. 4 and Table 1). HAADF-STEM shows uniformly distributed nanoparticles with a narrow size range and mean particle diameter of 1.1 (± 0.5 nm), while bright-field TEM shows that the ordered mesopore architecture of the Al-SBA-15(4) support is preserved, with elemental analysis (in STEM configuration) confirming the presence of both Pd and Al throughout the pore network. Palladium metal dispersions were used to estimate average particle diameters, assuming a spherical morphology, for comparison against similar Pd loadings on mesoporous alumina and SBA-15 supports [22] and [24]. Table 1 shows that far higher dispersions and smaller nanoparticles were achieved over the Al-SBA-15(4) support than pure SBA-15 or meso- Al_2O_3 materials, as reported for Pt on Al-SBA-15 [40]. The palladium oxidation state within Pd/Al-SBA-15(4) was probed by XPS, with both metal and oxide observed (Fig. S3). The surface PdO content quantified in Table 1 was significantly higher than that observed for comparable metal loadings over mesoporous silica or alumina, consistent with the higher palladium dispersion. We have previously noted that these properties are closely correlated over alumina supports [24], and Fig. 5 confirms that in this respect, palladium nanoparticles on Al-SBA-15(4) behave akin to those on pure meso- Al_2O_3 .

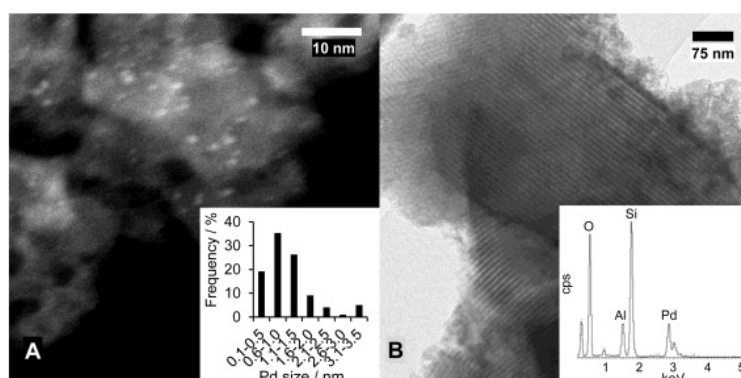


Fig. 4. (A) Representative HAADF-STEM image of Pd/Al-SBA-15(4) with Pd particle size distribution derived from 100 particles shown inset; and (B) Bright field TEM image with corresponding EDX spectrum shown inset (unlabelled peaks correspond to C and Cu from the sample grid).

Table 1. Physicochemical properties of Pd/Al-SBA-15(4) versus Pd/meso- Al_2O_3 and Pd/SBA-15.

Support	Pd loading (wt.%) ^a	Pd dispersion (%) ^b	Pd particle size (nm) ^b	Surface PdO content (%) ^c
Al-SBA-15(4)	0.77	88 (± 1)	1.0 (± 0.1)	44.3 (± 4.2)
meso- Al_2O_3 ^d	0.74	74 (± 1)	1.5 (± 0.1)	21.9 (± 2.2)
SBA-15 ^e	0.89	52 (± 1)	2.3 (± 0.1)	6.0 (± 0.1)

- ICP analysis.
- Pulse chemisorption assuming stoichiometry of 1:2 CO: Pd.
- PdO% from fitted Pd 3d XP spectra.
- From reference [24].
- From reference [22].

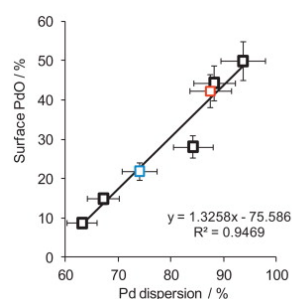


Fig. 5. Linear correlation between palladium dispersion (from CO titration) and surface PdO content (from XPS fitting) for Pd/Al-SBA-15(4) and mesoporous Al_2O_3 (taken from reference [21]). Red and blues data points represent 0.77 wt.% Pd/Al-SBA-15 and 0.74 wt.% Pd/meso- Al_2O_3 respectively. (For interpretation of the references to colour in this figure legend, the reader is referred to the web version of this article.)

3.2. Cinnamyl alcohol selox

The catalytic activity of Pd/Al-SBA-15 towards the aerobic selox of cinnamyl alcohol was determined in order to benchmark its performance against Pd/SBA-15 or Pd/meso- Al₂O₃ [22], [23] and [24], and thus assess support effects. Identical reaction conditions, including stirring speed, reaction vessel dimensions, O₂ flow rate and temperature, were selected to match our previous studies and facilitate direct comparison of catalysts in the absence of bulk mass transport limitations. The mass-normalised initial rate of cinnamyl alcohol selox for Pd/Al-SBA-15(4) was exceptional, being twice that observed over the pure meso- Al₂O₃ support, and almost 20 times that obtained for Pd/SBA-15 (Table 2, Fig. S4). Although Pd/Al-SBA-15(4) affords a higher rate of cinnamyl selox than obtained for the Pd/meso- Al₂O₃ catalyst, their corresponding turnover frequencies (TOFs) per surface PdO sites are almost identical (~13,500 h⁻¹), suggesting a common active species and palladium-support interaction; the principal impact of the more highly ordered Al-SBA-15 support is simply to increase the density of such PdO sites. A similar explanation has been advanced for the superior electrocatalytic performance of Pt supported on ordered mesoporous CMK-3 versus a disordered wormhole-like mesoporous carbon for ethanol oxidation and oxygen reduction [48]. If cinnamyl selox activity was solely a function of the concentration of PdO present at the surface of oxidised palladium nanoparticles, then one might expect a common TOF for all three catalysts, independent of support type. In fact, the TOF for the Pd/SBA-15 catalyst was only 6,108 h⁻¹. Since the morphology of Al-SBA-15 is identical to that of its SBA-15 parent, such different TOFs are not easily explained by differing mass-transport properties, but rather suggest a palladium-silica interaction distinct from that obtained with the alumina-grated surface. We propose that the enhanced activity and TOFs for alumina versus silica supported palladium reflects a superior ability to disperse and preserve smaller, and hence more heavily oxidised, PdO nanoparticles during cinnamyl selox. A gradation of 'PdO' active centres may thus exist over oxide supports, which though all formally Pd²⁺, may differ in their dimensionality and thus reducibility [18]. The unsaturated allylic aldehyde, cinnamaldehyde, was the dominant product for all three catalysts (formed with ~70% selectivity), with 3-phenylpropan-1-ol and trans- β -methylstyrene the major by-products (both ~14% after 3 h reaction), with styrene and ethylbenzene minor by-products (<5%) via cinnamaldehyde decarbonylation and subsequent hydrogenation (Fig. S5).

Table 2. Cinnamyl alcohol selox over Pd/Al-SBA-15(4) versus Pd/meso- Al₂O₃ and Pd/SBA-15.

Catalyst	Conversion (%) ^a	Cinnamaldehyde (%) ^b	Initial activity (mmol gPd ⁻¹ h ⁻¹) ^b	TOF (h ⁻¹) ^c
Pd/Al-SBA-15	95 (100)	64 (66)	53260	13600
Pd/meso- Al ₂ O ₃ ^d	56 (98)	39 (66)	25595	13391
Pd/SBA-15 ^e	21 (41)	16 (31)	2950	6108

a. Conversion and cinnamaldehyde selectivity after 30 min (and 3 h in parentheses) flowing O₂.

b. Calculated over the initial 20–30 min for conversions <50%.

c. Normalised to PdO active site density (XPS).

d. From reference [20].

e. From reference [18].

3.3. Operando XAS studies of cinnamyl alcohol selox

Additional laboratory studies of cinnamyl alcohol selox over Pd/Al-SBA-15 revealed rapid on-stream deactivation in under 10 min when a static oxygen pressure was maintained above the reaction solution, instead of oxygen flowing through the solution (Fig. S6 and 7). We therefore undertook time-resolved, operando Pd K-edge XAS measurements on the 0.77 wt.% Pd/Al-SBA-15 catalyst to assess the interplay between static versus flowing oxygen and the corresponding oxidation state of palladium nanoparticles. Previous work on the vapour phase oxidation of crotyl alcohol, an analogue of cinnamyl alcohol, has shown the importance of high oxygen concentrations in maintaining steady state catalytic selox over palladium nanoparticles and single crystals [19], [21] and [23]. Normalised Pd K-edge XAS spectra of as-prepared Pd/Al-SBA-15 in toluene, and after 1 h cinnamyl alcohol selox under static or flowing oxygen, are presented in Fig. 6. XANES of the as-prepared catalyst exhibits a significant white line consistent with the presence of substantial PdO (~74% PdO from fitting to standards). After 1 h selox under flowing oxygen (i.e. a higher concentration of dissolved oxygen) there is little visible change in the operando XANES spectra, and indeed fitting suggests around 66% of palladium remains as PdO. In contrast, after 1 h reaction under static oxygen, significant

changes are apparent in the XANES consistent with reduction to palladium metal, with only 41% PdO retained. Flowing oxygen thus helps preserve palladium in the +2 oxidation state under full selox reaction conditions.

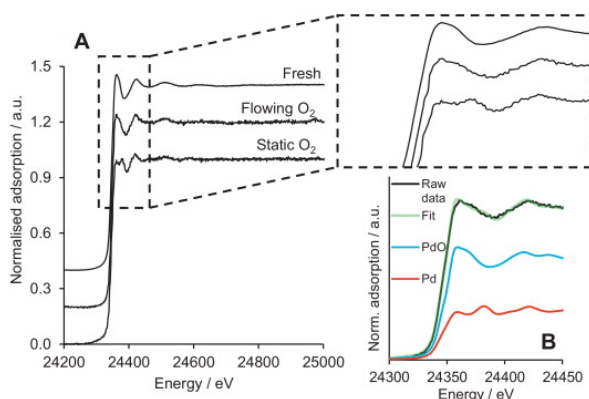


Fig. 6. (A) Operando XANES of the as-prepared Pd/Al-SBA-15 in toluene (superior data quality reflects the average of 10 spectra), and after 1 h cinnamyl alcohol selox reaction under static or flowing O_2 (single spectrum); (B) linear combination fitted XANES spectrum of Pd/Al-SBA-15 under flowing O_2 .

The time-dependent evolution of palladium oxidation state and concomitant impact upon instantaneous selox activity during the first 2 h of reaction are closely correlated (Fig. 7A). Under static conditions, the concentration of PdO, determined in solution during cinnamyl alcohol oxidation, falls rapidly during the first 20 min reaction before reaching a plateau, mirrored by a sharp drop in catalyst reactivity which reaches a low, stable selox rate. When this reaction is repeated with an oxygen flow introduced before alcohol addition, the initial high [PdO] is maintained for the first 20 min of the reaction, coincident with a constant, high selox rate. Longer reaction times result in a monotonic decrease in both palladium oxide concentration and activity, although neither parameter falls to the low values observed under static oxygen.

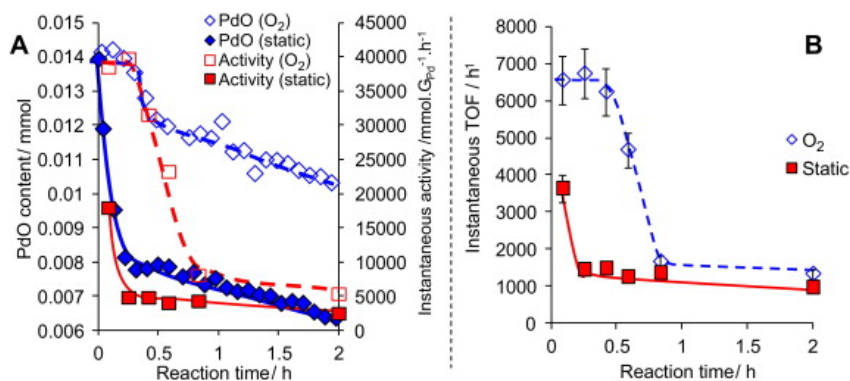


Fig. 7. (A) Impact of flowing versus static oxygen on palladium oxidation state and catalytic activity of Pd/Al-SBA-15 during liquid phase cinnamyl alcohol selox. (B) Evolution of corresponding TOFs (normalised per PdO surface sites) as a function of reaction time (250 mg catalyst and 84 mmol alcohol substrate). Note, lower TOFs relative to laboratory batch conditions reflect heating losses from circulating solution during transfer between cell and reservoir.

If catalyst deactivation quantitatively tracked palladium reduction, then the corresponding instantaneous TOFs (per PdO site) should remain constant throughout reaction under static and flowing oxygen. Fig. 7B reveals that a constant TOF is only observed for the first 30 min under flowing oxygen, before a steep decrease to the same low steady state value obtained under static conditions, indicating the genesis of a new, common, poorly active species, which *vide supra*, is assigned to Pd^0 . Palladium metal is known to favour aldehyde decarbonylation [49], resulting in catalyst self-poisoning by strong-bound hydrocarbons and CO [20] and [21]. Carbonaceous residues may irreversibly block subsequent alcohol adsorption, while CO can serve as both a reversibly adsorbed site-blocker and reductant [50] and [51]. Our operando measurements confirm that on-stream deactivation occurs via a transition from highly active and selective cinnamyl alcohol oxidation over PdO, to the slow and unselective conversion of cinnamyl alcohol

over metallic Pd with attendant self-poisoning by undesired by-products of decarbonylation. Although the low flow of oxygen (at atmospheric pressure) employed in this study was insufficient to fully suppress in situ catalyst reduction, it is clear that the local concentration of (dissolved) oxygen is critical in regulating the rate of Pd/Al-SBA-15 deactivation. This is consistent with the oxidative dehydrogenation reaction mechanism generally accepted for allylic alcohol selox [52]. Fig. 7 shows that maintaining palladium catalysts in a high oxidation state during operando liquid phase selox is essential for optimising their activity, in agreement with our observations of gas phase crotyl alcohol selox [17] and [19]. Throughout our research on the selective oxidation of allylic alcohols, whether in the liquid or gas phase, and under oxygen-rich or deficient conditions, a direct correlation between selox activity and palladium oxide concentration determined in situ has been observed [16], [18] and [21], hence there is no convincing evidence for catalyst deactivation during allylic alcohol selox due to palladium ‘over-oxidation’.

The preceding XANES analysis is supported by EXAFS fitting of the as-prepared 0.77 wt.% Pd/Al-SBA-15 catalyst in toluene, and after 2 h cinnamyl alcohol selox under static or flowing oxygen (Fig. 8). An excellent fit to the as-prepared Pd/Al-SBA-15 catalyst was obtained for a mix of PdO and Pd (Table S1), with Pd-O nearest neighbours at 2.02 Å the dominant scatterers. We propose the as-prepared catalyst comprised a metallic palladium core encapsulated by a multilayer palladium oxide shell, akin to Pd/SBA-15 [22]. The extremely low Pd–Pd 1st shell coordination number at 2.7 Å (and absence of longer range shells expected for Pd metal), and presence of Pd–Pd scatterers at 2.68 Å and 3.04 Å consistent with ‘bulk-like’ PdO, indicate a relatively thick oxide shell and small metal core compared to the silica analogue, in keeping with the higher selox activity of Pd/Al-SBA-15.

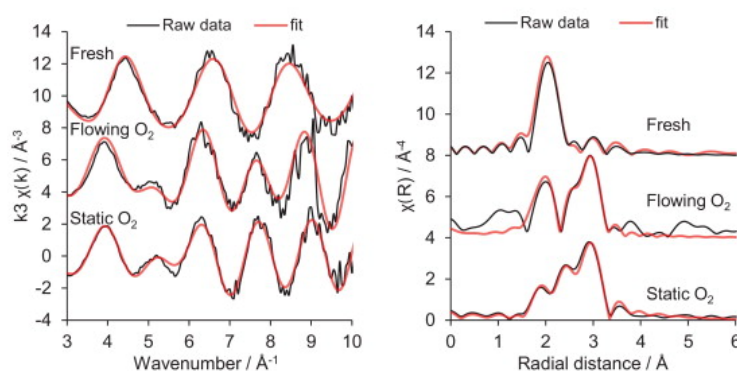


Fig. 8. k^3 -weighted EXAFS data and corresponding Fourier transforms and fits for as-prepared 0.77 wt.% Pd/Al-SBA-15 in toluene and after 1 h cinnamyl alcohol selox reaction under static O_2 or flowing O_2 .

EXAFS spectra of Pd/Al-SBA-15 in solution following 2 h reaction under either static or flowing oxygen could only be successfully fitted by including a third phase, palladium carbide (Fig. 8 and Table S1); fits to a two-phase mixture of oxide, metal or carbide were poor (Fig. S8 and Table S2). Palladium carbide is known to form via surface-mediated reactions with gaseous hydrocarbons at ambient temperature [53] and [54] or CO decomposition, resulting in a characteristic Pd–C scattering feature ~ 2.16 Å and concomitant palladium lattice expansion [55]. Good fits were obtained only though including additional shells, Pd–C at 2.16 Å and an expanded Pd–Pd shell at ~ 2.84 Å [54]. Carbide formation from metallic palladium can usually be discerned through subtle shifts in the first and second XANES features due to the interaction between the excited 1s photoelectron with empty 5p and 4f orbitals [55] and [56], however the complex mixture of oxide/metal/carbide present under reaction conditions prohibited such observations. The first shell Pd–Pd coordination number of the metallic phase observed operando under either oxygen environment of ~ 1.8 is essentially identical to that of the fresh catalyst in toluene, suggesting a common metallic core. This leads us to hypothesise that the carbide represents an amorphous surface phase, formed as a result of in situ PdO reduction (apparent from the fall in first shell Pd–O coordination number from 3.2 under toluene, to 1.8 and 1.4 under flowing and static oxygen respectively) and subsequent carbon laydown over metallic surface sites. The concomitant rise in selectivity to trans- β -methylstyrene from $\sim 5\%$ after 10 min reaction to $\sim 15\%$ after 2 h (and to a lesser degree styrene), associated with a partial switchover from oxidative dehydrogenation to Csingle bondO cleavage pathways, could be the trigger for carbide formation [49].

It is interesting to consider whether dissolved oxygen could re-oxidise palladium nanoparticles reduced in situ, and thus regenerate catalytic selectivity. We have only ever observed palladium re-oxidation and associated reactivation during vapour phase selectivity experiments [17] and [18] at (i) significantly higher temperatures (140 °C) than those used in the present liquid phase study (90 °C), and (ii) local oxygen concentrations far exceeding those employed during our solution phase experiments (mol fraction^{vapour} = 0.025 versus mol fraction^{toluene} = 0.0009 [57]), or following a deliberate post-reaction 500 °C calcination treatment [22] wherein the calcined catalyst exhibits a comparable PdO content to that of fresh catalysts. The forcing conditions required to re-oxidise palladium nanoparticles suggest that the deactivated metal/carbide surfaces may be poisoned by strongly adsorbed hydrocarbons, and hence are resistant to mild re-oxidation treatments – this hypothesis is supported by comparing C 1s XP spectra of fresh and spent 0.42 wt.% Pd/SBA-16 catalysts (Fig. S9). Pd(0) reoxidation back to PdO thus likely requires thermal activation; this poses a problem for solution phase regeneration, with Henry's Law dictating a decrease in oxygen solubility with increasing solution temperature. We therefore predict that palladium re-oxidation at 90 °C would only be feasible under $p_{O_2} > 20$ bar for which the mol fraction of dissolved oxygen rises to 0.025 [57].

4. Conclusions

Deposition of ultrathin alumina films on mesoporous SBA-15 silica provides an effective route to the synthesis of a highly ordered, high-area catalyst support exhibiting alumina-like surface properties. The resulting composite Al-SBA-15 support facilitates enhanced dispersion of palladium nanoparticles, and thus a greater proportion of surface PdO than either mesoporous silica or alumina for comparable palladium loadings. Consequently, Pd/Al-SBA-15 exhibits superior activity in the liquid phase aerobic selective oxidation of cinnamyl alcohol to cinnamaldehyde than Pd/SBA-15 or Pd/meso- Al₂O₃. Turnover frequency analysis indicates that ultrathin and bulk alumina surfaces generate higher levels of a common (PdO) active species than can be achieved over silica, indicating significant metal-support interactions. Operando XAS measurements reveal strong correlations between the palladium oxidation state and selectivity which identify rapid, on-stream PdO reduction as the major deactivation pathway, which can be ameliorated by an increase in the local oxygen partial pressure. PdO reduction opens up undesired C–O bond cleavage and decarbonylation pathways (with attendant loss of cinnamaldehyde selectivity), with the resulting hydrocarbon and CO by-products liberated driving surface palladium carbide formation. Knowledge of the redox chemistry of palladium nanoparticles under reaction conditions, and advantages of employing a nanostructured Al-SBA-15 support in generating and maintaining high surface PdO concentrations is critical to the design of next-generation palladium-derived catalysts for energy efficient alcohol selectivity and process optimisation.

Acknowledgement

We thank the EPSRC (EP/E046754/1; EP/G007594/2; and EP/F009488/1) for financial support, a Leadership Fellowship (A.F.L.) and studentships (L.J.D. and A.M.) and Diamond Light Source for beamtime (SP7668-1). K.W. acknowledges the Royal Society for the award of an Industry Fellowship. Electron microscopy access was provided through the Leeds EPSRC Nanoscience and Nanotechnology Research Equipment Facility (LENNF) (EP/F056311/1).

Supplementary data to this article is available online

References

- [1] S.S. Cheng, J.Y. Liu, K.H. Tsai, W.J. Chen, S.T. Chang. Chemical composition and mosquito larvicidal activity of essential oils from leaves of different *Cinnamomum osmophloeum* provenances. *J. Agr. Food Chem.*, 52 (2004), pp. 4395–4400.
- [2] G.O. Onawunmi. Evaluation of the antimicrobial activity of citral. *Lett. Appl. Microbiol.*, 9 (1989), pp. 105–108.
- [3] T. Hattori, Y. Suzuki, O. Uesugi, S. Oi, S. Miyano. Cationic palladium(II) complex-catalyzed [2 + 2] cycloaddition and tandem cycloaddition-allylic rearrangement of ketene with aldehydes: an improved synthesis of sorbic acid. *Chem. Commun.* (2000), pp. 73–74.
- [4] C. Mercier, P. Chabardes. Organometallic chemistry in industrial vitamin A and vitamin E synthesis. *Catal. Org. React.*, 62 (1994), p. 213.
- [5] J.H. Clark. Green chemistry: challenges and opportunities. *Green Chem.*, 1 (1999), pp. 1–8.
- [6] R.A. Sheldon. Fundamentals of green chemistry: efficiency in reaction design. *Chem. Soc. Rev.*, 41 (2012), pp. 1437–1451.
- [7] A. Corma, H. Garcia. Supported gold nanoparticles as catalysts for organic reactions. *Chem. Soc. Rev.*, 37 (2008), pp. 2096–2126.

- [8] X.Y. Liu, R.J. Madix, C.M. Friend. Unraveling molecular transformations on surfaces: a critical comparison of oxidation reactions on coinage metals. *Chem. Soc. Rev.*, 37 (2008), pp. 2243–2261.
- [9] T. Takeji, T. Akita, I. Nakamura, T. Fujitani, M. Okumura, K. Okazaki, J. Huang, T. Ishida, M. Haruta. Chapter one-heterogeneous catalysis by gold. C.G. Bruce, C.J. Friederike (Eds.), *Advances in Catalysis*, Academic Press (2012), pp. 1–126. Article. PDF (5065 K).
- [10] C.P. Vinod, K. Wilson, A.F. Lee. Recent advances in the heterogeneously catalysed aerobic selective oxidation of alcohols. *J. Chem. Technol. Biotechnol.*, 86 (2011), pp. 161–171.
- [11] S.E. Davis, M.S. Ide, R.J. Davis. Selective oxidation of alcohols and aldehydes over supported metal nanoparticles. *Green Chem.*, 15 (2013), pp. 17–45.
- [12] T. Balcha, J.R. Strobl, C. Fowler, P. Dash, R.W.J. Scott. Selective aerobic oxidation of crotyl alcohol using AuPd core-shell nanoparticles. *ACS Catal.*, 1 (2011), pp. 425–436.
- [13] T. Hara, M. Ishikawa, J. Sawada, N. Ichikuni, S. Shimazu. Creation of highly stable monomeric Pd(II) species in an anion-exchangeable hydroxy double salt interlayer: application to aerobic alcohol oxidation under an air atmosphere. *Green Chem.*, 11 (2009), pp. 2034–2040.
- [14] R.A. Sheldon, I. Arends, A. Dijkstra. New developments in catalytic alcohol oxidations for fine chemicals synthesis. *Catal. Today*, 57 (2000), pp. 157–166. Article. PDF (239 K).
- [15] S.S. Stahl. Palladium oxidase catalysis: selective oxidation of organic chemicals by direct dioxygen-coupled turnover. *Angew. Chem. Int. Edit.*, 43 (2004), pp. 3400–3420.
- [16] A.F. Lee, K. Wilson. Structure-reactivity correlations in the selective aerobic oxidation of cinnamyl alcohol: in situ XAFS. *Green Chem.*, 6 (2004), pp. 37–42.
- [17] A.F. Lee, C.V. Ellis, J.N. Naughton, M.A. Newton, C.M.A. Parlett, K. Wilson. Reaction-driven surface restructuring and selectivity control in allylic alcohol catalytic aerobic oxidation over Pd. *J. Am. Chem. Soc.*, 133 (2011), pp. 5724–5727.
- [18] C.V. Gaskell, C.M.A. Parlett, M.A. Newton, K. Wilson, A.F. Lee. Redox-controlled crotyl alcohol selective oxidation: in situ oxidation and reduction dynamics of catalytic Pd nanoparticles via synchronous XANES/MS. *ACS Catal.*, 2 (2012), pp. 2242–2246.
- [19] C.M.A. Parlett, C.V. Gaskell, J.N. Naughton, M.A. Newton, K. Wilson, A.F. Lee. Operando synchronous DRIFTS/MS/XAS as a powerful tool for guiding the design of Pd catalysts for the selective oxidation of alcohols. *Catal. Today*, 205 (2013), pp. 76–85.
- [20] A.F. Lee, Z. Chang, P. Ellis, S.F.J. Hackett, K. Wilson. Selective oxidation of crotyl alcohol over Pd(1 1 1). *J. Phys. Chem. C*, 111 (2007), pp. 18844–18847.
- [21] A.F. Lee, J.N. Naughton, Z. Liu, K. Wilson. High-pressure XPS of crotyl alcohol selective oxidation over metallic and oxidized Pd(1 1 1). *ACS Catal.*, 2 (2012), pp. 2235–2241.
- [22] C.M.A. Parlett, D.W. Bruce, N.S. Hondow, M.A. Newton, A.F. Lee, K. Wilson. Mesoporous silicas as versatile supports to tune the palladium-catalyzed selective aerobic oxidation of allylic alcohols. *Chem. Cat. Chem.*, 5 (2013), pp. 939–950.
- [23] C.M.A. Parlett, D.W. Bruce, N.S. Hondow, A.F. Lee, K. Wilson. Support-enhanced selective aerobic alcohol oxidation over Pd/mesoporous silicas. *ACS Catal.*, 1 (2011), pp. 636–640.
- [24] C.M.A. Parlett, K. Wilson, D.W. Bruce, N.S. Hondow, A.F. Lee. Selective oxidation of allylic alcohols over highly ordered Pd/meso- Al₂O₃ catalysts. *Catal. Commun.* (2013).
- [25] J. Lu, S. Behtash, M. Faheem, A. Heyden. Microkinetic modeling of the decarboxylation and decarbonylation of propanoic acid over Pd(1 1 1) model surfaces based on parameters obtained from first principles. *J. Catal.*, 305 (2013), pp. 56–66.
- [26] B. Karimi, A. Zamani, S. Abedia, J.H. Clark. Aerobic oxidation of alcohols using various types of immobilized palladium catalyst: the synergistic role of functionalized ligands, morphology of support, and solvent in generating and stabilizing nanoparticles. *Green Chem.*, 11 (2009), pp. 109–119.
- [27] Y.T. Chen, Z. Guo, T. Chen, Y.H. Yang. Surface-functionalized TUD-1 mesoporous molecular sieve supported palladium for solvent-free aerobic oxidation of benzyl alcohol. *J. Catal.*, 275 (2010), pp. 11–24.
- [28] Z.C. Ma, H.Q. Yang, Y. Qin, Y.J. Hao, G.A. Li. Palladium nanoparticles confined in the nanocages of SBA-16: enhanced recyclability for the aerobic oxidation of alcohols in water. *J. Mol. Catal. A-Chem.*, 331 (2010), pp. 78–85.

- [29] C.-J. Jia, F. Schuth. Colloidal metal nanoparticles as a component of designed catalyst. *Phys. Chem. Chem. Phys.*, 13 (2011), pp. 2457–2487.
- [30] D.Y. Zhao, J.L. Feng, Q.S. Huo, N. Melosh, G.H. Fredrickson, B.F. Chmelka, G.D. Stucky. Triblock copolymer syntheses of mesoporous silica with periodic 50 to 300 angstrom pores. *Science*, 279 (1998), pp. 548–552.
- [31] F. Kleitz, S.H. Choi, R. Ryoo. Cubic Ia3d large mesoporous silica: synthesis and replication to platinum nanowires, carbon nanorods and carbon nanotubes. *Chem. Commun.* (2003), pp. 2136–2137.
- [32] S.F.J. Hackett, R.M. Brydson, M.H. Gass, I. Harvey, A.D. Newman, K. Wilson, A.F. Lee. High-activity, single-site mesoporous Pd/Al₂O₃ catalysts for selective aerobic oxidation of allylic alcohols. *Angew. Chem. Int. Edit.*, 46 (2007), pp. 8593–8596.
- [33] A.Y. Stakheev, L.M. Kustov. Effects of the support on the morphology and electronic properties of supported metal clusters: modern concepts and progress in 1990. *Appl. Catal. A-Gen.*, 188 (1999), pp. 3–35.
- [34] S.J. Tauster. Strong metal-support interactions. *Accounts Chem. Res.*, 20 (1987), pp. 389–394.
- [35] K. Hayek, R. Kramer, Z. Paal. Metal-support boundary sites in catalysis. *Appl. Catal. A-Gen.*, 162 (1997), pp. 1–15.
- [36] M.V. Landau, E. Dafa, M.L. Kaliya, T. Sen, M. Herskowitz. Mesoporous alumina catalytic material prepared by grafting wide-pore MCM-41 with an alumina multilayer. *Micropor. Mesopor. Mat.*, 49 (2001), pp. 65–81.
- [37] M. Baca, E. de la Rochefoucauld, E. Ambroise, J.M. Krafft, R. Hajjar, P.P. Man, X. Carrier, J. Blanchard. Characterization of mesoporous alumina prepared by surface alumination of SBA-15. *Micropor. Mesopor. Mat.*, 110 (2008), pp. 232–241.
- [38] P. Madhusudhan Rao, A. Wolfson, S. Kababya, S. Vega, M.V. Landau. Immobilization of molecular H₃PW₁₂O₄₀ heteropolyacid catalyst in alumina-grafted silica-gel and mesostructured SBA-15 silica matrices. *J. Catal.*, 232 (2005), pp. 210–225.
- [39] X. Sheng, Y. Zhou, Y. Zhang, Y. Duan, Z. Zhang, Y. Yang. Immobilization of 12-Tungstophosphoric acid in alumina-grafted mesoporous LaSBA-15 and its catalytic activity for alkylation of o-xylene with styrene. *Micropor. Mesopor. Mat.*, 161 (2012), pp. 25–32.
- [40] Y. Duan, Y. Zhou, Y. Zhang, X. Sheng, S. Zhou, Z. Zhang. Effect of aluminum modification on catalytic properties of PtSn-based catalysts supported on SBA-15 for propane dehydrogenation. *J. Nat. Gas Chem.*, 21 (2012), pp. 207–214. Article. PDF (337 K). Citing articles (9).
- [41] E.J.M. Hensen, D.G. Poduval, P. Magusin, A.E. Coumans, J.A.R. Veen. Formation of acid sites in amorphous silica–alumina. *J. Catal.*, 269 (2010), pp. 201–218. Article. PDF (1105 K).
- [42] Q.-Q. Hao, Y.-H. Zhao, H.-H. Yang, Z.-T. Liu, Z.-W. Liu. Alumina grafted to SBA-15 in supercritical CO₂ as a support of cobalt for Fischer–Tropsch synthesis. *Energy Fuels*, 26 (2012), pp. 6567–6575.
- [43] S.J. Pennycook, L.A. Boatner. Chemically sensitive structure-imaging with a scanning-transmission electron-microscope. *Nature*, 336 (1988), pp. 565–567.
- [44] NIST X-ray Photoelectron spectroscopy database. NIST standard reference database 20, Version 3.5 (2003) <http://srdata.nist.gov/xps/>. Accessed January 2012.
- [45] P.J. Cumpson, M.P. Seah. Elastic scattering corrections in AES and XPS. II. Estimating attenuation lengths and conditions required for their valid use in overlayer/substrate experiments. *Surf. Interface Anal.*, 25 (1997), pp. 430–446.
- [46] A.F. Lee, C.V. Ellis, K. Wilson, N.S. Hondow. In situ studies of titania-supported Au shell-Pd core nanoparticles for the selective aerobic oxidation of crotyl alcohol. *Catal. Today*, 157 (2010), pp. 243–249.
- [47] V. Maurice, I. Bennour, S. Zanna, L.H. Klein, P. Marcus. Modifications and growth mechanisms of ultrathin aluminum oxide films on NiAl in water. *J. Phys. Chem. C*, 114 (2010), pp. 7132–7140.
- [48] S.Q. Song, Y.R. Liang, Z.H. Li, Y. Wang, R.W. Fu, D.C. Wu, P. Tsiakaras. Effect of pore morphology of mesoporous carbons on the electrocatalytic activity of Pt nanoparticles for fuel cell reactions. *Appl. Catal. B-Environ.*, 98 (2010), pp. 132–137. Article. PDF (532 K).
- [49] M. Bowker, L. Cookson, J. Bhantoo, A. Carley, E. Hayden, L. Gilbert, C. Morgan, J. Counsell, P. Yaseneva. The decarbonylation of acetaldehyde on Pd crystals and on supported catalysts. *Appl. Catal. A-Gen.*, 391 (2011), pp. 394–399.
- [50] T. Maillet, C. Solleau, J. Barbier Jr., D. Duprez. Oxidation of carbon monoxide, propene, propane and methane over a Pd/Al₂O₃ catalyst effect of the chemical state of Pd. *Appl. Catal. B-Environ.*, 14 (1997), pp. 85–95.

- [51] T. Lear, N.G. Hamilton, D. Lennon. The application of temperature-programmed desorption, adsorption isotherms and temperature-programmed oxidation to investigate the interaction of CO with alumina-supported palladium catalysts. *Catal. Today*, 126 (2007), pp. 219–227.
- [52] M. Besson, P. Gallezot. Selective oxidation of alcohols and aldehydes on metal catalysts. *Catal. Today*, 57 (2000), pp. 127–141. Article. PDF (212 K).
- [53] M.W. Tew, M. Janousch, T. Huthwelker, J.A. van Bokhoven. The roles of carbide and hydride in oxide-supported palladium nanoparticles for alkyne hydrogenation. *J. Catal.*, 283 (2011), pp. 45–54. Article. PDF (1371 K).
- [54] M. Bauer, R. Schoch, L. Shao, B. Zhang, A. Knop-Gericke, M. Willinger, R. Schlögl, D. Teschner. Structure–activity studies on highly active palladium hydrogenation catalysts by X-ray absorption spectroscopy. *J. Phys. Chem. C*, 116 (2012), pp. 22375–22385.
- [55] M.A. Newton, M.D. Michiel, A. Kubacka, M. Fernández-García. Combining time-resolved hard X-ray diffraction and diffuse reflectance infrared spectroscopy to illuminate CO dissociation and transient carbon storage by supported Pd nanoparticles during CO/NO cycling. *J. Am. Chem. Soc.*, 132 (2010), pp. 4540–4541.
- [56] J.A. McCaulley. In situ X-ray absorption spectroscopy studies of hydride and carbide formation in supported palladium catalysts. *J. Phys. Chem.*, 97 (1993), pp. 10372–10379.
- [57] K. Fischer, M. Wilken. Experimental determination of oxygen and nitrogen solubility in organic solvents up to 10 MPa at temperatures between 298 K and 398 K. *J. Chem. Thermodyn.*, 33 (2001), pp. 1285–1308.